J. Fluid Mech. (2004), *vol.* 514, *pp.* 355–383. © 2004 Cambridge University Press
DOI: 10.1017/S0022112004000400 Printed in the United Kingdom

Intrusive gravity currents and internal gravity wave generation in stratified fluid

By MORRIS R. FLYNN AND BRUCE R. SUTHERLAND

Department of Mathematical and Statistical Sciences, University of Alberta, Edmonton, AB, Canada, T6G 2G1

(Received 1 May 2003 and in revised form 10 May 2004)

The excitation of internal gravity waves by fluid intrusions that propagate along the interface between a uniform upper layer and a uniformly stratified lower layer is examined by way of laboratory experiments. Intrusions are generated using a simple lock-release apparatus. Experiments are conducted in which the density gradient of the uniformly stratified layer, the density jump across the interface and the density difference between the lock fluid and the uniform upper layer are varied.

In all cases, the fluid intrusions travelled at a constant speed. The forcing imparted by the generated internal gravity waves did not deform the intrusion head or significantly retard the intrusion's rate of forward advance. For a limited range of density parameters, good agreement was obtained between the experimental data and the two-layer analytical theory of J. Y. Holyer & H. E. Huppert (*J. Fluid Mech.* vol. 100 (1980), pp. 739–767) which provides estimates for the intrusion speed and depths of penetration into the upper and lower layers. Internal gravity wave excitation is due to the initial collapse of the lock fluid and the forcing imparted by the head of the intrusion. Waves are visualized and their amplitudes measured using 'synthetic schlieren'.

The vertical flux of horizontal momentum due to internal gravity wave excitation is related to measurable properties of the fluid intrusion. This analysis suggests that outflows produced by tall convective storms that travel along the tropopause may excite non-hydrostatic internal gravity waves in the stratosphere whose momentum flux, at least during the transient generation time, is comparable to that of waves generated by topographic forcing.

1. Introduction

Gravity currents (also known as density currents or buoyancy currents) and internal gravity waves are ubiquitous phenomena in the atmosphere and ocean. The former arise when fluid of one density propagates horizontally into fluid of another density. Atmospheric manifestations of this phenomenon include thunderstorm outflows and sea breeze fronts (Simpson 1982, 1997). Most experimental and theoretical studies of gravity currents have examined the propagation of dense fluid along a rigid boundary beneath a uniform ambient (Keulegan 1957; Benjamin 1968; Simpson 1972; Britter & Simpson 1978; Simpson & Britter 1979; Huppert & Simpson 1980; Klemp, Rotunno & Skamarock 1994; D'Alessio *et al.* 1996; Hallworth *et al.* 1996; Härtel *et al.* 1997; Shin, Dalziel & Linden 2004). A gravity current that propagates along an interface within a stratified fluid we refer to as a fluid intrusion. These have been studied theoretically and experimentally by Holyer & Huppert (1980), Britter & Simpson (1981),

https://doi.org/10.1017/S0022112004000400 Published online by Cambridge University Press

D'Alessio *et al.* (1997), de Rooij (1999), de Rooij, Linden & Dalziel (1999), Mehta, Sutherland & Kyba (2002) and Sutherland, Kyba & Flynn (2004).

Internal gravity waves, which propagate within density stratified environments, play an important role in atmospheric circulation. For example, it is well known that the breakdown of internal gravity waves imparts a significant drag on the zonal winds (Lindzen 1981; Kida 1984; Gavrilov & Roble 1994; Becker & Schmitz 2002). Although the largest proportion of momentum transport by internal gravity waves is associated with those generated by topographic forcing (Fritts & Nastrom 1992), other dynamic excitation mechanisms can also result in significant momentum fluxes. In particular, convective forcing may represent the most important source of atmospheric internal gravity waves in the southern hemisphere and the tropics (Alexander, Holton & Durran 1995). Beres, Alexander & Holton (2002) have identified three means by which convective motion may excite waves (see also Mason & Sykes 1982; Clark, Hauf & Kuettner 1986; Fovell, Durran & Holton 1992). 'Quasi-stationary forcing' describes the generation of internal gravity waves by perturbations to the mean flow caused by the pressure field of a rising convective element. Because the element thereby acts as a 'fluidic' (i.e. non-rigid) obstacle, this mechanism is also known as the 'obstacle effect'. In the absence of a background mean flow, waves may be generated through the oscillatory deflection to the boundary of a stratified layer owing to the successive rising and falling of convective eddies. This scenario is similar to the experiments of Plumb & McEwan (1978) in which boundary deflections were established using mechanical means. The mechanism is therefore referred to as the 'mechanical oscillator effect'. The third means for wave excitation is the 'deep heating effect' which describes the generation of internal gravity waves due to the thermal forcing associated with the latent heat release within a convective storm. Internal gravity wave generation is thus due to fluid expansion; the wave's vertical wavelength is approximately twice that of the vertical extent through which heating occurs (Salby & Garcia 1987).

Whereas Clark *et al.* (1986) determined that a strong wind shear was required for the generation of strong internal gravity waves, Fovell *et al.* (1992) found that this was not the case when considering the deep convection associated with mesoscale convective storms, even though their analysis did not explicitly consider the 'deep heating effect'.

In addition to topographic and convective forcing, atmospheric internal gravity waves may also be generated by the vortices produced in an unstable parallel shear flow, a mechanism referred to as 'shear generation' (Lindzen 1974; Sutherland, Caulfield & Peltier 1994; Sutherland 1996; Sutherland & Linden 1998). Qualitatively, internal gravity waves are anticipated when the stratification of the strongly sheared region is low compared to that of the surrounding strongly stratified ambient as characterized by Richardson numbers less than and greater than 1/4, respectively.

Here, we initiate an idealized experimental study examining a novel variation of the convective and shear mechanisms for wave generation in which stratospheric internal gravity waves are excited by the propagation of a fluid intrusion along the tropopause, the boundary separating the weakly stratified troposphere (below) from the strongly stratified stratosphere (above). As demonstrated in figure 1, examples of such flows include laterally spreading anvil clouds, propagating high-level rope clouds that form by detaching from the leading edge of anvil clouds (Simpson 1997) and, more exotically, laterally spreading volcanic clouds (Rose *et al.* 2001).

Previous investigations into the generation of internal gravity waves in a uniformly stratified fluid by density-driven currents fall under two principal categories: those in

https://doi.org/10.1017/S0022112004000400 Published online by Cambridge University Press

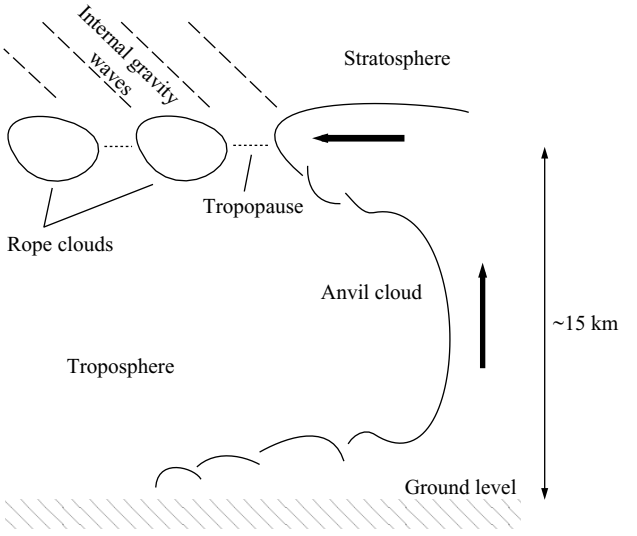


FIGURE 1. The ascent of a tall anvil cloud. When the mass of hot moist air reaches the tropopause, it may, under certain conditions, begin to spread laterally, giving rise to a fluid intrusion that propagates along the interface between a strongly stratified fluid (above) and a weakly stratified fluid (below).

which wave excitation is due to a bottom-propagating gravity current (Maxworthy *et al.* 2002; Ungarish & Huppert 2002) and those in which the current propagates at some intermediate depth (Schooley 1967; Wu 1969; Schooley & Hughes 1972; Manins 1976; Amen & Maxworthy 1980; Britter & Simpson 1981; Faust & Plate 1984; de Rooij 1999). In the experiments of Maxworthy *et al.* (2002), the gravity current was released using a standard lock-release apparatus. Direct excitation of internal gravity waves occurred when the current's velocity was below that of the linear mode-one long wave in the wave guide, a condition referred to by Maxworthy *et al.* (2002) as 'subcritical' (see also Long 1955). At this point, 'first-mode waves were formed which interacted with the head of the advancing gravity current to destroy the original front and to cause a succession of gravity-current heads' (Simpson 1982). In other words, a rhythmic coupling was established that alternately accelerated and decelerated the gravity current head. By contrast, no such behaviour has been observed in studies involving a non-stratified ambient for which the gravity current speed is constant over a horizontal distance of approximately ten lock-lengths (Simpson 1997).

Experiments involving the propagation of a homogeneous mixed region within a stratified fluid typically ignore boundary effects. Wu (1969) divided the gravitational collapse of the mixed region into three distinct stages: the 'initial' stage, during which the rate of collapse is constant, the 'principal' stage during which the collapse rate begins to decrease and the 'final' stage in which the mixed region becomes wedge-shaped and propagates so slowly that viscous effects become significant. Internal gravity waves are generated both above and below the collapsing mixed layer.

Whereas Wu (1969) did not observe a resonant interaction between the intrusion and the internal gravity waves, such behaviour was noted in the related study of Amen & Maxworthy (1980), for whom the initial height of the mixed region relative to the depth of the stratified ambient was notably larger. As in the experiments of Maxworthy *et al.* (2002), this interaction resulted in the irregular advance of the intrusion head.

https://doi.org/10.1017/S0022112004000400 Published online by Cambridge University Press

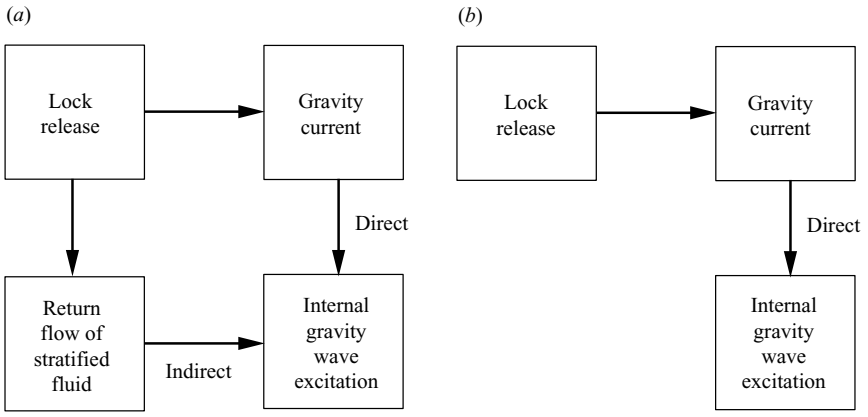


FIGURE 2. Comparison between the mechanisms of internal gravity wave excitation in the studies of (*a*) Wu (1969), Amen & Maxworthy (1980) and Maxworthy *et al.* (2002) and (*b*) the present study.

For both classes of experiment described above, internal gravity wave generation is due to two factors: direct excitation by the gravity current and indirect excitation associated with the return flow of stratified fluid that is established by the release of the lock (see figure 2*a*).

Experiments performed in the present study are different from those described above in two fundamental respects. They consider the behaviour of a fluid intrusion in a two-layer system in which the lower layer is uniformly stratified and the top layer is uniform in density. As in the investigations of Wu (1969), Amen & Maxworthy (1980) and Maxworthy *et al.* (2002), flow is established using a simple lock-release apparatus. In the present case, however, the lock fluid initially spans only the height of the uniform layer and the collapse of the mixed region therefore occurs strictly within non-stratified surroundings. Consequently, the collapse of the lock fluid does not induce a return flow in the stratified (lower) layer. As indicated in figure 2(*b*), internal gravity wave generation is due solely to the direct mechanism: forcing by the fluid intrusion. Whereas previous experiments are characterized by the appearance of columnar modes (internal gravity waves of infinite horizontal wavelength that are associated with a bulk flow of stratified fluid within a closed geometry), these features are only apparent in the present study when the forcing exerted by the fluid intrusion on the lower layer is relatively large. The excitation of columnar modes is undesirable because it effectively changes the mean density and velocity profiles in the region (Baines 1995).

Although the atmosphere's potential temperature and velocity profiles are more complicated than the corresponding background profiles considered in the present study, the experiments bear some resemblance to the interfacial flow phenomenon depicted in figure 1. In particular, although the experiments capture only Boussinesq dynamics, they nonetheless provide an important starting point for assessing the importance of thunderstorm outflows as sources of internal gravity waves given that the vertical extent over which wave forcing occurs in the atmospheric circumstance is small relative to the local scale height.

The paper is organized as follows: § 2 provides an overview of the analytic theory of Holyer & Huppert (1980) (here in after referred to as HH80) which describes the propagation of a fluid intrusion between two uniform layers. Simplifications to

https://doi.org/10.1017/S0022112004000400 Published online by Cambridge University Press

their original equations are derived by employing the Boussinesq approximation. In addition, the theory of de Rooij *et al.* (1999), which considers the behaviour of a fluid intrusion in a two-layer system under more restrictive conditions, will be discussed. The experimental set-up is summarized in § 3. Section 4 presents a comparison between the measured intrusion properties and those predicted by HH80. The behaviour of the internal gravity waves is analysed in § 5. Finally, § 6 considers the application of the experimental data to the atmospheric flow depicted in figure 1.

2. Theory

The behaviour of an inviscid gravity current propagating into a uniform ambient of depth h_T was considered theoretically by Benjamin (1968). Using conservation of mass and momentum, he demonstrated that for energy-conserving flows in which surface tension and mixing can be neglected, the current depth h_{gc} was half the total fluid depth ($h_{gc} = h_T/2$) and the current speed, v_{gc}, was given by

$$v_{gc} = \frac{1}{\sqrt{2}}\sqrt{g' h_{gc}}. \tag{2.1}$$

Here, we represent the reduced gravity by $g' = g(\rho_{gc} - \rho_0)/\rho_{00}$, in which g is the acceleration due to gravity, ρ_{gc} is the gravity current density, ρ_0 is the density of the ambient fluid and, in the Boussinesq approximation, ρ_{00} is a characteristic reference density that we take to equal ρ_0.

These results were extended by HH80 who derived equations describing the propagation of a fluid intrusion in a two-layer system consisting of uniform layers for which the interfacial thickness is vanishingly small. For non-dissipative intrusive flows, they obtained a coupled system of cubic polynomial equations for r_0 and r_1, the relative decrease in depth of the ambient fluid as it moves, respectively, above and below the intrusion. By invoking the Boussinesq approximation, this system of equations was simplified by Sutherland *et al.* (2004) who further derived approximate solutions from perturbation expansions about ϵ, measuring the relative density difference between the intrusion and the average density of the ambient. Explicitly, using the notation represented in figure 3, they defined

$$\epsilon = \frac{\rho_i - \bar{\rho}}{\rho_1 - \rho_0},$$

where

$$\bar{\rho} = \frac{h_1\rho_1 + h_0\rho_0}{h_T},$$

and $h_T = h_1 + h_0$.

The analysis presented here starts with the coupled polynomial equations (2.4) and (2.5) of Sutherland, Kyba & Flynn (2004). However, rather than determining perturbation solutions about $\epsilon = 0$, here we expand about a small parameter Γ representing the relative density difference between the intrusion and the upper layer. This is the relevant parameter for the experiments presented here because in the majority of our experiments the intrusion propagates with most of its bulk in the upper (uniform density) layer and with only weak penetration into the lower (stratified) layer. Thus, increasing Γ corresponds to increasing forcing of internal waves in the stratified fluid. (In the theory presented below, both layers of the ambient are assumed to have uniform density; but, if Γ is small, the current structure and speed should not depend on whether the lower layer is stratified.)

https://doi.org/10.1017/S0022112004000400 Published online by Cambridge University Press

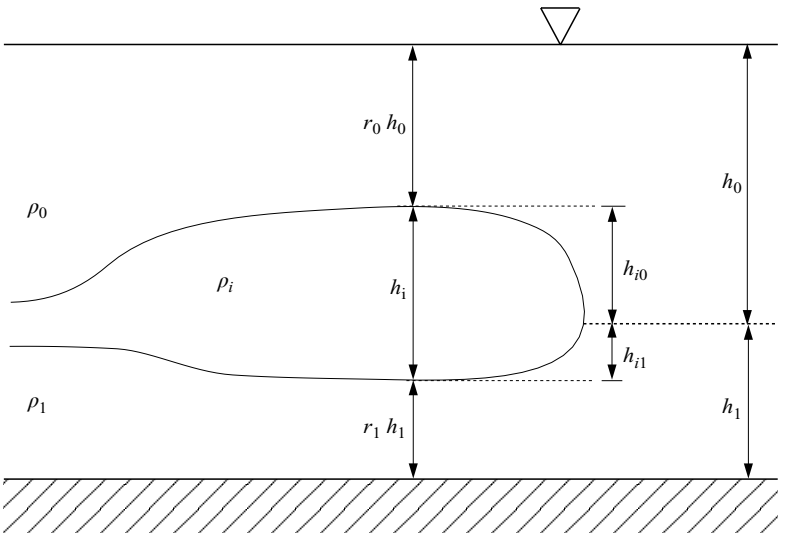


FIGURE 3. The propagation of a fluid intrusion of density ρ_i between uniform layers of densities ρ_0 (above) and ρ_1 (below).

We further require that Γ, unlike ϵ, be independent of the lower-layer depth, which should be insignificant in cases when the intrusion penetrates only weakly into the lower layer. We therefore define

$$\Gamma = \frac{\rho_i - \rho_0}{\rho_1 - \rho_0}. \tag{2.2}$$

For intrusions moving along the interface we must have $0 < \Gamma < 1$. Alternatively, we could have defined $\zeta = \Gamma - 1/2$, in which $\zeta = (\rho_i - \langle\rho_{10}\rangle)/(\rho_1 - \rho_0)$ and $\langle\rho_{10}\rangle = (\rho_1 + \rho_0)/2$ is the average of the densities on either flank of the interface. The parameter ζ was first introduced by de Rooij *et al.* (1999) in their study of intrusions in fluid with equal upper- and lower-layer depths. Here, we work with Γ because it is a more suitable perturbation parameter for the cases we are interested in, specifically, $0 \leqslant \Gamma \ll 1$.

We transform from the equations of Sutherland *et al.* (2004) involving ϵ to equations involving Γ using the relation

$$\epsilon = \Gamma - \frac{h_1}{h_T}.$$

As $\Gamma \to 0$, we find $r_0 = 1/2$ and $r_1 = 1$. We therefore find perturbation solutions by substituting $r_0 = 1/2 + \delta_0$ and $r_1 = 1 - \delta_1$ into the coupled cubic polynomial equations to give

$$\Gamma(1 + 2\delta_0)^2(1 - 2\delta_0) = 8H_1\delta_1(1 - \Gamma)(1 - \delta_1)^2 \tag{2.3}$$

and

$$\delta_0\Gamma(1 - 2\delta_0)^2 = 2\delta_1^2(H_1)^2(1 - \Gamma)(2\delta_1 - 1), \tag{2.4}$$

in which $H_1 = h_1/h_0$.

These equations are perturbed about small Γ by assuming $\delta_0 = \Gamma\delta_0{}^{(1)} + O(\Gamma^2)$ and $\delta_1 = \Gamma\delta_1{}^{(1)} + O(\Gamma^2)$. Substituting these into (2.3) and (2.4) and matching like powers of Γ, we thereby determine the heights, h_{i0} and h_{i1}, of the intrusion above and below

https://doi.org/10.1017/S0022112004000400 Published online by Cambridge University Press

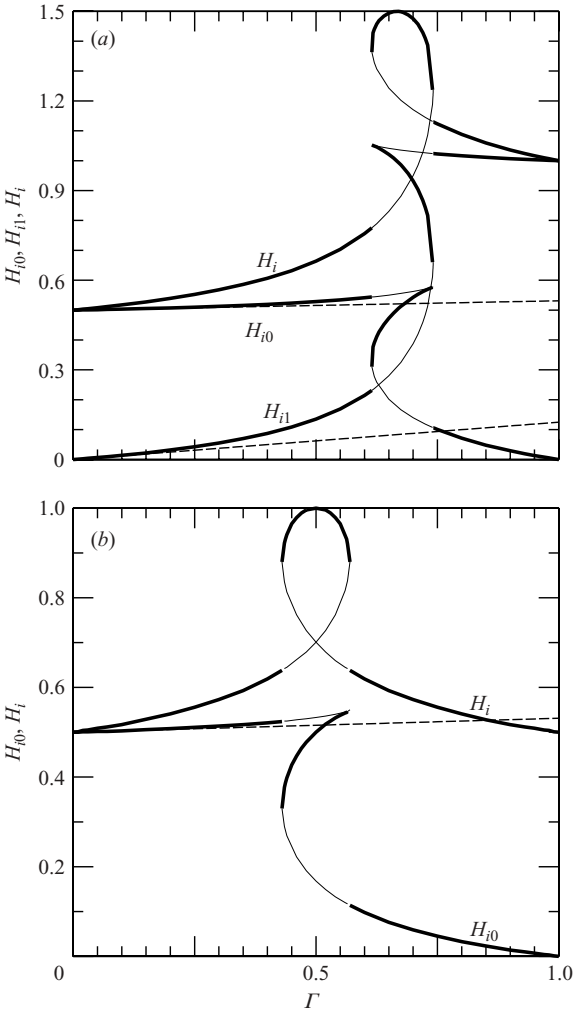


FIGURE 4. (*a*) Intrusion heights h_{i0}, h_{i1} and h_i (normalized by h_0) versus Γ for $h_1 = 2h_0$ and (*b*) h_{i0} and h_i (normalized by h_0) versus Γ for $h_1 = h_0$. In the intervals over which HH80 predicts non-unique solutions, the physically anticipated solution is denoted by the thick solid line. First-order perturbation expansions about $\Gamma = 0^+$ are indicated by the long dashed lines. (*a*) $H_1 = 2$. (*b*) $H_1 = 1$.

the interface, respectively. Relative to the upper-layer ambient depth, h_0, we find

$$H_{i0} \equiv \frac{h_{i0}}{h_0} = \tfrac{1}{2} + \tfrac{1}{32}\Gamma + O(\Gamma^2) \tag{2.5}$$

and

$$H_{i1} \equiv \frac{h_{i1}}{h_0} = \tfrac{1}{8}\Gamma + O(\Gamma^2). \tag{2.6}$$

Thus, for Γ sufficiently small, the total relative intrusion depth is $H_i \equiv H_{i0} + H_{i1} \simeq 1/2 + 5\Gamma/32$.

Figure 4 presents comparisons between the exact results of HH80 and the first-order perturbation expansions given by (2.5) and (2.6), the latter being represented

https://doi.org/10.1017/S0022112004000400 Published online by Cambridge University Press

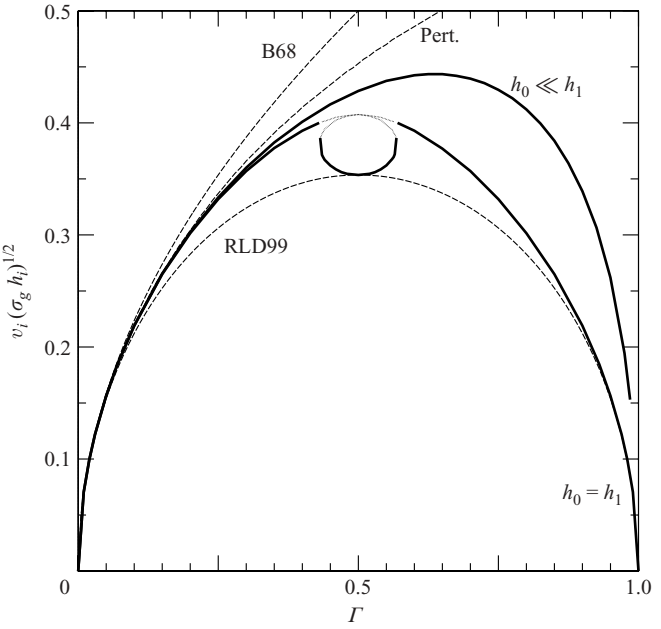


FIGURE 5. Predicted normalized intrusion velocities as a function of Γ. The thick curves plot the values in cases with $h_0 = h_1$ and $h_0 \ll h_1$, as indicated. In the former case, thin lines are drawn in the overlap region for values corresponding to non-maximal mass flux (see Sutherland *et al.* 2004). The curve labelled 'Pert.' is the second-order accurate perturbation approximation about $\Gamma = 0$, the curve labelled 'B68' is that predicted by Benjamin (1968), and the curve labelled 'RLD99' is that predicted by de Rooij *et al.* (1999).

by long-dashed lines. Note that the exact solution of HH80 has three solutions for a range of Γ. These are discussed in detail by Sutherland *et al.* (2004) but are irrelevant to the discussion here because they occur for sufficiently large Γ that they are outside the range of interest as represented by our perturbation parameter. In the asymmetric case with $H_1 = 2$ (typical of our experiments) and for $\Gamma \leqslant 0.2$, the leading-order perturbation theory gives 0.2% and 21.9% accuracy for H_{i0} and H_{i1}, respectively. Likewise, in the symmetric case $H_1 = 1$, the perturbed solutions reasonably estimate the exact behaviour for $\Gamma \lesssim 0.2$.

The intrusion speed is given generally by

$$v_i = r_0 \sqrt{2\Gamma \sigma g h_0 (1 - r_0)}, \tag{2.7}$$

in which $\sigma = (\rho_1 - \rho_0)/\rho_{00}$. For small Γ, we find

$$\frac{v_i}{\sqrt{\sigma g h_i}} = \sqrt{\tfrac{1}{2}}\Gamma\left(1 - \tfrac{3}{16}\Gamma + O(\Gamma^2)\right). \tag{2.8}$$

Figure 5 compares the leading-order perturbation solutions of (2.8) with the exact solutions of HH80 in the case with $h_0 = h_1$ and $h_0 \ll h_1$. In both cases, the approximate theory is accurate to within 0.5% of the exact result for $\Gamma \leqslant 0.2$.

We expect (2.8) should be equivalent to (2.1) in the limit $\Gamma \to 0$. Indeed, in this limit $v_i \to v_{gc}$, $h_i \to h_{gc}$ and $\sigma \Gamma g \to g'$. The correction terms in (2.8) reflect that the relative speed of the intrusion decreases as it penetrates more deeply into the lower layer. Figure 5 explicitly compares the formula derived by Benjamin (1968) (the curve labelled 'B68') with our formula for a two-layer fluid.

https://doi.org/10.1017/S0022112004000400 Published online by Cambridge University Press

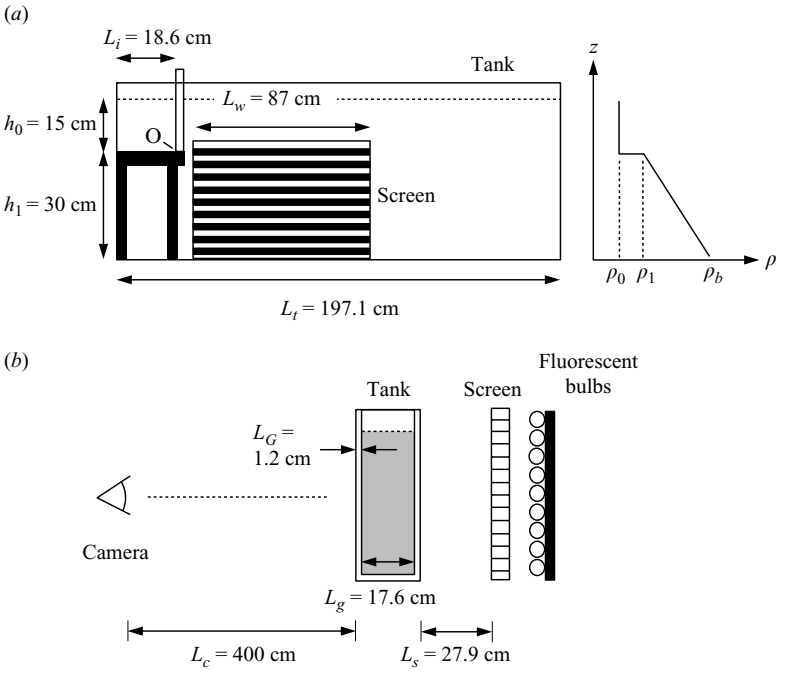


FIGURE 6. (*a*) Front view of the tank showing the lock-release mechanism by which intrusions are released along the interfacial layer. Also shown is a schematic representation of the density profile. For the purposes of our subsequent analysis, we place the origin of an (x, z) coordinate system at the point denoted by O. (*b*) Side view of the tank showing the relative positions of the grid of black and white lines, the tank and the CCD camera. (Figures not to scale.)

Also shown in figure 5 is a curve (denoted by 'RLD99') due to the analytic theory of de Rooij *et al.* (1999). Their model represents a simplification of HH80 in that they assume both layers are infinite in extent and hence effectively equal in depth. Their solution, which is applicable to both energy-conserving and dissipative currents, expresses v_i as an explicit function of ζ:

$$\frac{v_i}{\sqrt{\sigma g h_i}} = \tfrac{1}{2} Fr \sqrt{\frac{\rho_0}{\rho_i}} \sqrt{1 - 4\zeta^2} \simeq \tfrac{1}{2} Fr \sqrt{1 - 4\zeta^2} \equiv Fr \sqrt{\Gamma(1 - \Gamma)}. \tag{2.9}$$

Here the Froude number, Fr, is defined by requiring that the predicted solution approach that given by Benjamin (1968) and HH80 in the limit $\Gamma \to 0^+$. Specifically, we set $Fr = 1/\sqrt{2}$. As indicated by figure 5, the solution of de Rooij *et al.* (1999) is approximated well by (2.8) for $\Gamma \lesssim 0.2$.

3. Experimental methods

Experiments were performed in a glass tank of length 197.1 cm, width 19.9 cm wide and height 48.5 cm (see figure 6). A platform (height = 30 cm; length 19.6 cm) that spanned the width of the tank was installed at one end. The non-uniform density profile was established using a two-step process. First, a 30.0 cm deep layer of uniformly salt stratified fluid was added to the tank using the 'double bucket' technique (Oster 1965). Thus, the top of the stratified fluid was at the level of the top of the platform. A 15.0 cm deep layer of fresh or slightly saline water was then layered on

https://doi.org/10.1017/S0022112004000400 Published online by Cambridge University Press

top of the stratified fluid by trickling it through a sponge float. A traversing conductivity probe was used to measure the resulting density profile. The initial interfacial thickness was approximately 1 cm.

After filling the tank, a 0.4 cm thick gate was inserted between a pair of vertical glass guides to the level of the platform. Salt and a small amount of dye were then added to the lock fluid, after which it was made homogeneous by vigorous mixing for a period of approximately 15 s. The resulting fluid had a density ρ_i.

In total, 39 experimental runs were performed in which three parameters were varied: the strength of stratification of the lower layer, as measured by the squared buoyancy frequency, N^2; the relative density jump, σ, across the interface; and the relative density of the intrusion as measured by $\sigma_{i0} = (\rho_i - \rho_0)/\rho_{00} \equiv \sigma\Gamma$. Note that our definition of σ is the same as that for a two-layer fluid with uniform-density upper and lower layers. Here, however, ρ_1 is strictly taken to be the density immediately below the interface between the uniform and stratified layer.

Experiments were performed with N^2 ranging from $0.37\,\mathrm{s}^{-2}$ to $1.21\,\mathrm{s}^{-2}$ ($\pm 0.04\,\mathrm{s}^{-2}$), σ ranging from 0.0015 to 0.0102 (± 0.0001) and σ_{i0} ranging from 0.0005 to 0.0023 (± 0.0001). With these values, we find that the corresponding intrusion depth and speeds give typical Reynolds numbers of $\mathrm{Re} \simeq 1500$. As such, it is reasonable to neglect the role of viscosity in the dynamics of the fluid intrusion.

Our interest is in the response of the stratified layer to disturbances caused by intrusions for which the depth of penetration into the stratified (lower) layer is relatively small because this is most representative of the atmospheric flow depicted in figure 1 (Cotton & Anthes 1989). Hence, in the majority of experiments, $\rho_i < \langle \rho_{10} \rangle$ (i.e. $\sigma_{i0} < \sigma/2$). In this density regime, the forcing imparted by the fluid intrusion on the lower layer is insufficient to induce a significant bulk motion of stratified fluid. As described in § 1, such flows are undesirable because they may excite columnar modes.

Runs began by rapidly removing the gate from the tank. The lock fluid then collapsed to form an intrusion that propagated along (or in three extreme cases immediately below) the interfacial layer. The purpose of the platform was two-fold. It inhibited the vertical motion of the fluid intrusion during the initial collapse stage and thereby reduced the magnitude of the transient impulse delivered to the stratified layer. In addition, because the lock fluid extended only to the depth of the platform, and hence to the depth of the interface between the uniform and stratified fluid, no mean flow was induced as a result of stratified ambient fluid replenishing the collapsed lock fluid; only the unstratified ambient developed such a return flow.

The resulting fluid motions were recorded to video tape using a CCD camera located $L_c = 400$ cm in front of the tank. The zoom on the camera was set such that the field of view spanned a horizontal distance $L_w = 87$ cm with the gate at the left extremity of the field of view. The camera was connected to a computer running DigImage (Dalziel 1992), a robust image-processing program.

Experiments were run three-at-a-time. In other words, three intrusions, of progressively larger densities, were released in sequence where in each case, sufficient time (~ 10 min) was allowed between runs to permit the decay of the internal gravity waves in the stratified fluid. Although mixing and deposition of lock fluid at the interface resulted in successively broader interfacial thicknesses between runs, separate experiments showed that the depth of this mixed region was sufficiently smaller than the intrusion depth that this variation in the density profile had negligible effect.

The internal gravity waves that appeared in the stratified (lower) layer were visualized using 'synthetic schlieren', the properties of which are described in detail in Sutherland *et al.* (1999). The technique exploits variations in the index of refraction

https://doi.org/10.1017/S0022112004000400 Published online by Cambridge University Press

with salinity in order to visualize and measure the deflection of light rays as they travel through stratified fluid of spatially and temporally varying density gradient. In the present case, the internal gravity waves were visualized by measuring the distortion of an image of evenly spaced 0.5 cm thick horizontal black and white lines placed $L_s = 27.9$ cm behind the tank (see figure 6*b*). Assuming that the wave field is spanwise uniform (a reasonable approximation given the symmetry of the lock-release mechanism), it is possible to relate the change in the squared buoyancy frequency, ΔN^2, to the apparent vertical displacement of the lines, Δz, which under typical conditions, can be measured to within 0.002 cm. Explicitly,

$$\Delta N^2 \simeq -\alpha \Delta z, \tag{3.1}$$

where α depends upon the refractive indices of air, water and glass as well as L_s, the inside width of the tank, L_g, and the tank wall thickness, L_G (see figure 6*b*). For the present study, $\alpha = 6.4\,\mathrm{cm^{-1}\,s^{-2}}$. The resulting change in the vertical density gradient is then expressed in terms of the change in the squared buoyancy frequency, ΔN^2.

In addition to measuring the apparent displacement of a point from its original position, we may also compute the displacement that occurs during a short time interval, Δt (typically 0.1 s to 0.2 s). Hence, it is possible to estimate the time derivative of the ΔN^2 field, N_t^2, from

$$N_t^2 \simeq -\alpha \Delta z / \Delta t. \tag{3.2}$$

Internal gravity waves were observed in all cases except the three experiments with the weakest stratification for which $N^2 = 0.37\,\mathrm{s^{-2}}$. For these three experimental runs, the absence of observed waves is primarily an artefact of the synthetic schlieren technique: for a wave of fixed amplitude and spatial structure, the apparent displacement of the horizontal lines, Δz, is proportional to N^3. Hence, the signal from internal gravity waves can be detected and enhanced above noise levels only if N is sufficiently large.

4. Fluid intrusions

4.1. *Qualitative observations*

Gravity currents propagating in stratified media are subject to interactions with internal gravity waves whenever v_i is less than approximately $v_{LW} = N h_T/\pi$, the velocity of the longest linear mode-one wave that can exist in a uniformly stratified fluid of depth h_T (Maxworthy *et al.* 2002). Indeed, the simple calculation in Appendix A shows that symmetric intrusions in uniformly stratified fluid typically exist in a subcritical regime, in which they excite internal waves. (In contrast, bottom-propagating currents in a uniformly stratified ambient are supercritical if their density is sufficiently large, as can be done without restriction in theory.) Generally speaking, however, strong interactions are noted only when the magnitude of forcing is large. For example, in the study of Amen & Maxworthy (1980), $(h_i/h_T)_{t=0} \geqslant 0.40$ and a strong internal gravity wave-intrusion interaction was observed. By contrast, no such interaction developed in the experiments of Wu (1969) for whom $(h_i/h_T)_{t=0} = 0.25$. In the present study, we primarily consider fluid intrusions with $0 \leqslant \Gamma \ll 1$ and hence whose relative depth of penetration into the stratified layer, h_{i1}/h_1, is small. This is demonstrated for example by figure 7 which shows a representative image of the fluid intrusion head. Consistent with the analysis of Faust & Plate (1984) and de Rooij (1999), we find that no rhythmic coupling between the intrusion and the internal gravity waves occurs and that over the domain of interest ($0 \leqslant x \leqslant L_w$), the intrusion

https://doi.org/10.1017/S0022112004000400 Published online by Cambridge University Press

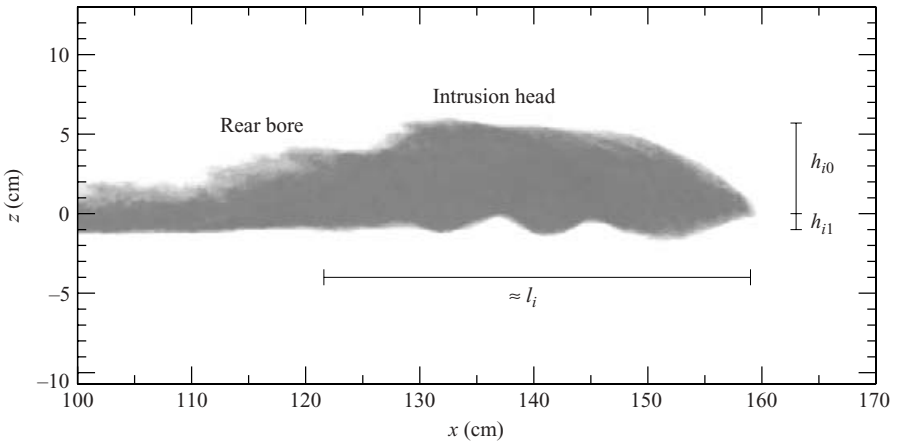


FIGURE 7. Image of the intrusion head for the experiment in which $N^2 = 0.67\,\mathrm{s}^{-2}$, $\sigma = 0.0038$ and $\sigma_{i0} = 0.0006$ ($\Gamma = 0.16$). The interface corresponds to the line $z = 0$ cm. The distances h_{i0}, h_{i1} and l_i are as indicated.

behaves as a slumping gravity current; v_i and h_i are approximately constant. In all cases, experiments are terminated before the intrusion's motion becomes self-similar.

The image shown in figure 7 is similar to figure 3(*c*) of Rottman & Simpson (1983). In particular, we note that when the return flow of non-stratified fluid reaches the tank wall, its reflection generates a forward-propagating rear bore that travels behind the intrusion head. Because the lock fluid does not extend into the stratified (lower) layer initially, no rear bore is excited along the underside of the intrusion (e.g. see Moodie 2002), though in some experiments undulating waves are evident along the lower interface of the intrusion.

4.2. *Determination of v_i, h_{i0}, h_{i1}, l_i and ω_i*

As described in Mehta, Sutherland & Kyba (2002), v_i was determined from horizontal time series of the digitized experimental images. Values for h_{i0} and h_{i1} were found from time series constructed along the vertical slice $x \simeq L_l = 18.6$ cm. Measurements were made roughly half-way between the leading and trailing edges of the intrusion head. In those experiments in which undular patterns were observed along the underside of the intrusion, h_{i1} was measured half-way between an undular peak and an undular trough. For the intrusion depicted in figure 7, for example, $h_{i0} = 5.7 \pm 0.2$ cm whereas $h_{i1} = 1.0 \pm 0.2$ cm.

Vertical time series along $x \simeq L_l = 18.6$ cm were also employed in determining l_i, the horizontal extent of the intrusion head. More precisely, l_i corresponds to the distance between the intrusion's typically sharp tip and the projected location at which the height of the intrusion head is equal to the height of the trailing tail. For example, figure 7 shows an intrusion for which $l_i = 37.2 \pm 5.0$ cm. Errors associated with l_i are due to the development of the rear bore and billows along the top and back of the intrusion head, both of which make it difficult to determine the precise location at which the trailing tail begins. From l_i, we can estimate characteristic values for ω_i, the frequency associated with the forcing imparted by the intrusion. Explicitly,

$$\omega_i = 2\pi \frac{v_i}{l_i}. \tag{4.1}$$

https://doi.org/10.1017/S0022112004000400 Published online by Cambridge University Press

4.3. *Flow instabilities*

Figure 7 shows the development of a series of undular patterns along the underside of the intrusion head. These undulations were noted in 19 of the 39 trials and are believed to result from a weak Kelvin–Helmholtz instability. They were also noted in the studies of Sutherland *et al.* (2004), who considered the propagation of a fluid intrusion between uniform layers, and Dugan, Warn-Varnas & Piacsek (1976), who developed a numerical model describing the gravitational collapse of a mixed region in a stratified ambient. Generally speaking, the undulations were observed in runs for which σ was relatively small and σ_{i0} was relatively large. Because v_i increases with ρ_i, the stress imparted by the intrusion on the fluid below the interface and the undulation amplitude, A_u, are expected to increase with σ_{i0}. Conversely, as $\sigma - \sigma_{i0}$ increases, a larger amount of energy is required to lift fluid at or near the interfacial layer. Therefore, A_u is expected to decrease with increasing σ in circumstances where $\rho_i < \langle \rho_{10} \rangle$.

These observations can be formalized by computing the interfacial Richardson number, *Ri*, defined as (see equation (1) of Wu 1969)

$$Ri = \frac{1}{16}\left(\frac{\Delta\rho}{\rho_{00}}\right)\left(\frac{gh_i}{v_i^2}\right). \tag{4.2}$$

Along the lower flank of the intrusion, $\Delta\rho/\rho_{00} = \sigma - \sigma_{i0}$ whereas along the upper flank, $\Delta\rho/\rho_{00} = \sigma_{i0}$. Generally speaking, undulations are observed along the intrusion's lower flank when *Ri* is less than 1/4. Because the density difference is smaller between the intrusion and ambient across the upper flank, the instability may grow to such a large amplitude that it overturns, forming billows.

4.4. *Comparison with Holyer & Huppert (1980)*

Figure 8 shows measured values of H_{i0} and H_{i1} as a function of Γ. In 36 of 39 experiments, $\rho_i < \rho_1$, and so $\Gamma < 1$. In three experiments, however, the intrusion was sufficiently dense that its bulk propagated below the interface and well within the stratified lower-layer ambient. We plot results for these experiments with values $\Gamma = 1$.

For comparison, figure 8 also shows theoretical curves determined from HH80's coupled system of cubic polynomials for the case where $h_0 \ll h_1$. Also presented are the first-order perturbation expansions given by (2.5) and (2.6).

Experimental values for H_{i0} are effectively independent of Γ and N^2; the theory of HH80 moderately overpredicts the observed data. Their model provides a reasonable, albeit somewhat depressed, estimate of the trend exhibited by the experimental data shown in figure 8(*b*) for $\Gamma \lesssim 0.75$. Theoretical values typically underpredict experimental values by 25 to 50%. For relatively dense intrusions ($\Gamma \gtrsim 0.75$), the depth of penetration becomes dependent on the strength of stratification: strongly stratified layers inhibit the vertical motion of the intrusion more effectively than those that are weakly stratified. These results suggest that, insofar as the dynamics of the intrusion are concerned, the stratification of the lower layer is not particularly important when $\Gamma \lesssim 0.75$. Thereafter, h_{i1} becomes dependent on N^2 and the dynamics influencing the intrusion's motion are more complicated than those considered by HH80. This observation is consistent with the analysis of Faust & Plate (1984) who considered the propagation of a fluid intrusion within a uniformly stratified ambient and who likewise found that two-layer theory poorly predicts their propagation.

The normalized velocity is shown as function of Γ in figure 9(*a*). Consistent with the results demonstrated in figure 8(*b*), the experimental data show reasonably good agreement with HH80's theory for $\Gamma \lesssim 0.75$. Little variation of $v_i/\sqrt{\sigma g h_i}$ with N^2

https://doi.org/10.1017/S0022112004000400 Published online by Cambridge University Press

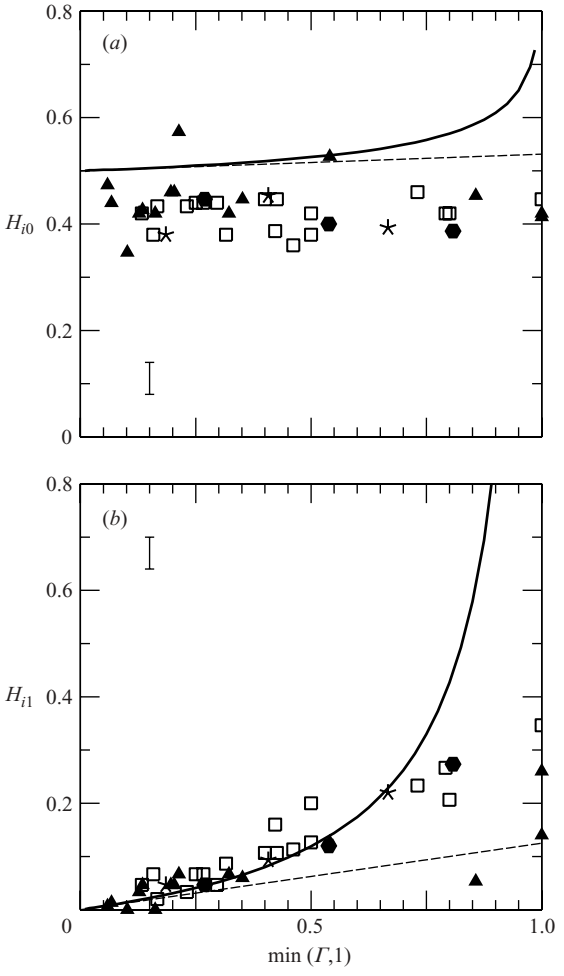


FIGURE 8. Normalized depth of penetration into the (*a*) upper and (*b*) lower layers. Data point types are ⬣, $N^2 = 0.37\,\mathrm{s}^{-2}$; □, $N^2 \simeq 0.67\,\mathrm{s}^{-2}$; ∗, $N^2 = 0.92\,\mathrm{s}^{-2}$; ▲, $N^2 \simeq 1.17\,\mathrm{s}^{-2}$. The solid and long dashed lines, respectively, indicate the full solutions predicted by HH80 and the first-order perturbation theory approximation to these solutions. The error bars denote the typical measurement uncertainty.

is observed; within experimental error, v_i is a function of Γ alone. Explicitly, from figure 9(*b*), we find that

$$\frac{v_i}{\sqrt{\sigma g h_i}} \propto \Gamma^{0.32\pm0.02}, \qquad \Gamma \leqslant 0.75. \tag{4.3}$$

The strength of the agreement between the experimental results and the two-layer model of HH80 suggests that the excitation of internal gravity waves does not extract a significant portion of the intrusion's horizontal momentum. This result is consistent with the numerical analysis of Ungarish & Huppert (2002) who, in modelling the slumping stage of the bottom-propagating gravity current experiments by Maxworthy *et al.* (2002), showed that internal waves extracted considerably less potential energy than the gravity current. In contrast, de Rooij (1999), observed significant interactions between symmetric intrusions in stratified fluids and the internal waves they generated,

https://doi.org/10.1017/S0022112004000400 Published online by Cambridge University Press

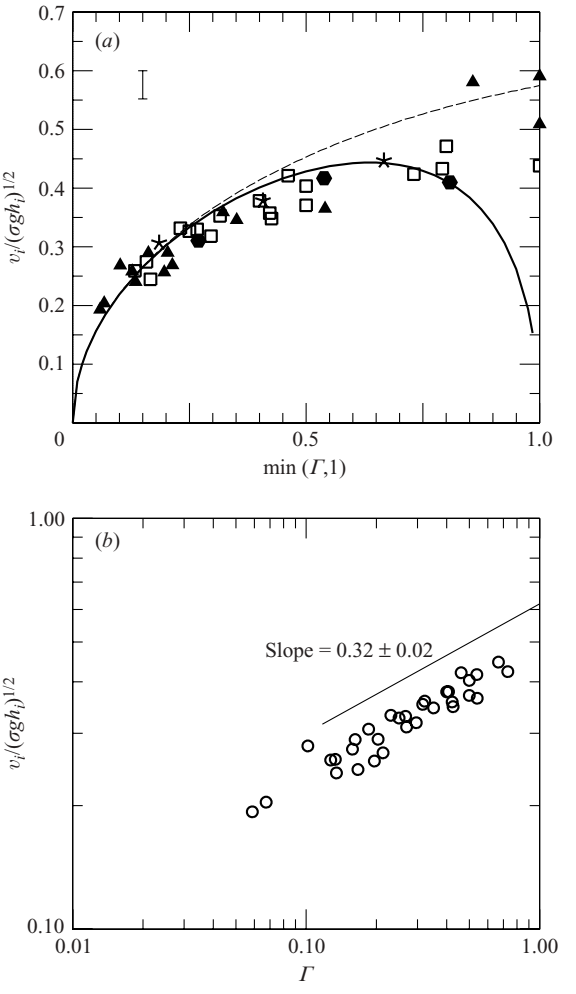


FIGURE 9. (*a*) Normalized intrusion velocity as a function of Γ. Data point and line types are as indicated in figure 8. The error bar denotes the typical measurement uncertainty. (*b*) Log–log plot of the same data, but plotted only for those experiments with $\Gamma \leqslant 0.75$. The slope of the (vertically offset) best-fit line is indicated.

estimating that energy extraction by waves in a typical experiment resulted in a 71% decrease in the intrusion speed. Waves are not so energetic in our study because the intrusion's depth of penetration into the stratified layer is initially zero and typically remains small throughout an experimental run.

We observe significant excitation of columnar modes only when $\Gamma \gtrsim 0.75$. In these cases, the character of the intrusion changes and the agreement between theory and experiment is poor for two reasons. First, the intrusion penetrates more deeply into the lower layer, and therefore its speed is dependent upon the value of N^2 and not just ρ_1. Second, columnar modes are larger amplitude and so interact more strongly with the intrusion in a way that retards its progress. Unfortunately, the experimental apparatus employed in this study is not well suited to distinguishing the relative importance of these two effects.

https://doi.org/10.1017/S0022112004000400 Published online by Cambridge University Press

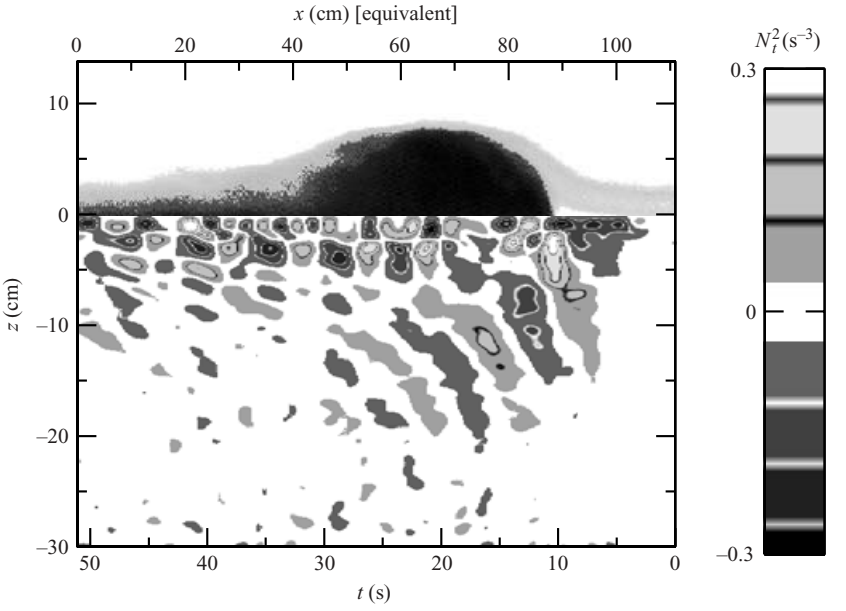


FIGURE 10. Composite time series along the vertical slice $x/L_l = 0.99$ corresponding to the experiment for which $N^2 = 1.17\,\mathrm{s}^{-2}$, $\sigma = 0.0037$ and $\sigma_{i0} = 0.0020$ ($\Gamma = 0.54$). The equivalent horizontal scale is indicated by the top axis.

5. Internal gravity waves

5.1. *Qualitative observations*

Time series of the N_t^2 field were constructed along 15 equally spaced columns ranging between $x \simeq 10\,\mathrm{cm}$ and 35 cm to the right of the gate. For $x \gtrsim 35\,\mathrm{cm}$, upward propagating internal gravity waves reflecting from the bottom of the tank significantly interfered with the downward propagating waves. The time series were Fourier filtered to remove noise due to signal degradation and high-frequency thermal fluctuations in the air space between the camera and the tank.

Figure 10 shows a composite vertical time series along the vertical slice $x = 18.4\,\mathrm{cm} \simeq L_l$ for a particular experimental run. The shear forces exerted by the fluid intrusion generate a region of intense isopycnal distortion immediately below the intrusion head. The internal gravity waves that appear below this region are relatively regular in spatial/temporal structure. The wave amplitude decreases with vertical distance from the wave source owing to the combined effects of viscous attenuation and wave dispersion. Because the intrusion speed is approximately constant, figure 10 is roughly equivalent to a 'snapshot' image with a horizontal dimension as indicated. In performing the Galilean translation from t to x, we apply $v_i = 2.2\,\mathrm{cm\,s}^{-1}$, not $v_{igw} = \omega/k_x = 3.0\,\mathrm{cm\,s}^{-1}$ in which ω and k_x represent the characteristic internal gravity wave frequency and horizontal wavenumber, respectively. Because the speeds of wave and intrusion propagation are not equal, figure 10 cannot be regarded as a 'true' snapshot image. Nonetheless, it suggests that there is a correlation between the horizontal length scale of the internal gravity waves and the head of the fluid intrusion. This idea is explored in more detail in § 5.3.

https://doi.org/10.1017/S0022112004000400 Published online by Cambridge University Press

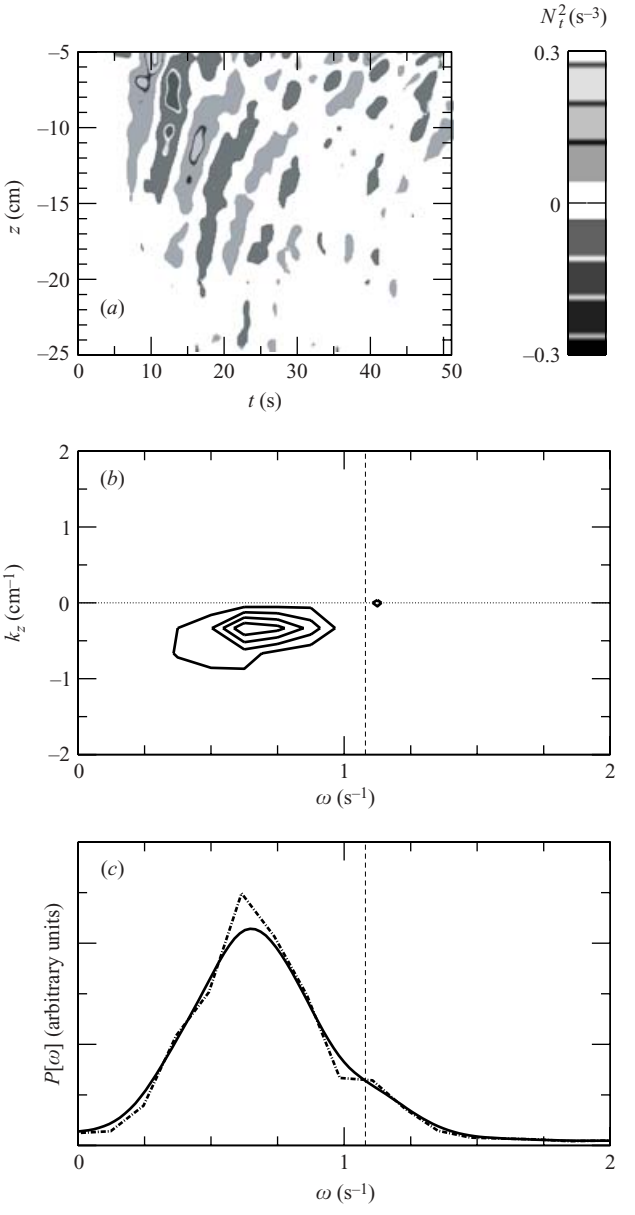


FIGURE 11. (*a*) Vertical time series of the N_t^2 field (see also figure 10). (*b*) The unsmoothed average power spectrum. (*c*) The ω profile corresponding to (b). The dashed-and-dotted line denotes the unsmoothed profile whereas the solid line denotes the smoothed profile. In both (*b*) and (*c*), the N value ($N = 1.08\,\mathrm{s}^{-1}$) for this particular experimental run is indicated by the vertical dashed line.

5.2. *Determination of ω, k_x and A_ξ*

Estimates of ω and k_x were obtained by applying a Fourier analysis similar to that described in Dohan & Sutherland (2003). Consider for example figure 11(*a*), in which the image from figure 10 is reproduced over the truncated vertical range $-25 \leqslant z \leqslant -5\,\mathrm{cm}$. The spectrum (in $\omega - k_z$ space) corresponding to this image was

https://doi.org/10.1017/S0022112004000400 Published online by Cambridge University Press

averaged with the spectra from the 14 other vertical time series from which the arithmetic mean spectrum shown in figure 11(*b*) was obtained. The ω profile depicted in figure 11(*c*) was computed by summing over k_z in the average spectrum. This profile was subsequently smoothed using a Gaussian smoothing procedure that employed a bin size of $0.1\,\mathrm{s}^{-1}$. Although the smoothing routine changes the profile's peak value, it does not significantly alter the location of the maximum, which in the present case appears at $\omega \simeq 0.65\,\mathrm{s}^{-1}$. We consider this the characteristic value of ω for the internal gravity wave field generated in this particular case.

We did not compute values for k_z from figure 11(*b*) because the vertical scale of the internal gravity waves was comparable with the vertical extent of the field of view. Consequently, horizontal time series of the N_t^2 field were reconstructed by combining data from 27 equally spaced vertical time series ranging from $x \simeq 5\,\mathrm{cm}$ to $x \simeq 75\,\mathrm{cm}$. Estimates of k_x were derived by computing the associated power spectrum (in $k_x - \omega$ space) then averaging this spectrum over ω (see figure 12*a–c*). The k_x profile was subsequently smoothed using a Gaussian smoothing procedure having a bin size of $0.05\,\mathrm{cm}^{-1}$. Although characteristic values for ω could be determined from power spectra such as that shown in figure 12(*b*), these estimates would be less reliable than those derived directly from the vertical time series owing to the additional step associated with the reconstruction of the horizontal time series from the vertical time series. In addition, because the wave envelope is narrower in figure 12(*a*) as compared to figure 11(*a*), the peaks in the corresponding power spectrum are less pronounced.

Knowing N, ω and k_x, values for k_z and $\Theta = \cos^{-1}(\omega/N)$, the theoretical angle which lines of constant phase form with respect to the vertical, were determined using the dispersion relation for internal gravity waves (see e.g. Lighthill 1978). Consistent with the study of Wu (1969), we observe some evolution of the internal gravity wave field over the course of a particular experiment as characterized by an increase in Θ with x. We are primarily interested in the behaviour of the internal gravity wave field in the relatively brief period immediately following the initial transient collapse of the lock fluid during which wave reflection off the bottom of the tank can be neglected. Hence, we consider the waves to be represented well by characteristic values for ω and k_x. In particular, the Fourier analysis technique described above is robust in that it is insensitive to the contribution of transient internal gravity waves excited during the initial collapse stage in which lock fluid of density ρ_i overshoots its point of neutral density and pushes into the stratified layer. For example, if in figure 11(*b*) the average power spectrum included only those vertical time series for which $x \simeq 19\,\mathrm{cm}$ to $35\,\mathrm{cm}$, we would find that $\omega \simeq 0.61\,\mathrm{s}^{-1}$. This result is within 6% of the value determined from figure 11(*c*).

More caution is required, however, when considering the wave amplitude, $A_{N_t^2}$, which is determined from the vertical time series of the N_t^2 field. Explicitly, $A_{N_t^2}$ is measured by computing ΔI, the maximum difference in pixel intensity between an adjacent wave trough and wave crest. The wave amplitude is then computed as follows

$$A_{N_t^2} = \frac{\Delta I}{\Delta I_M} \widehat{A_{N_t^2}},$$

where $\Delta I_M = 512$ and $\widehat{A_{N_t^2}}$ represents the threshold amplitude. For example, in generating figure 10, a threshold amplitude of $\widehat{A_{N_t^2}} = 0.3\,\mathrm{s}^{-3}$ is employed. Significant variability in $A_{N_t^2}$ exists near the lock-release point, indicating that the measurement technique is sensitive to the forcing of the stratified layer during the initial collapse stage. As this transient signature decays, however, the measured value for $A_{N_t^2}$ obtains

https://doi.org/10.1017/S0022112004000400 Published online by Cambridge University Press

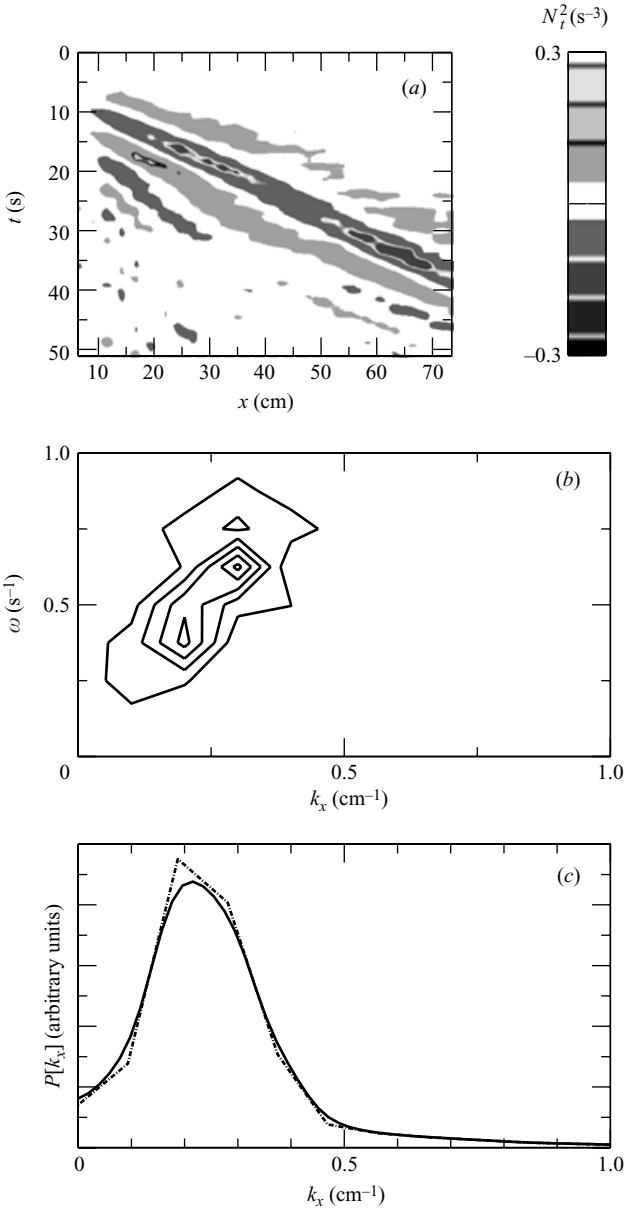


FIGURE 12. (*a*) Time series of the N_t^2 field along the horizontal slice $z/h_{i1} = -2.0$ for the experimental run described in figures 10 and 11. (*b*) The power spectrum corresponding to (*a*). (*c*) The k_x profiles as derived from (*b*). Line types are as indicated in figure 11*c*.

a more or less constant value subject to variations of approximately 20%. As such, characteristic values for $A_{N_t^2}$ were determined from time series corresponding to $x \simeq L_l = 18.6$ cm. Furthermore, because the wave amplitude decreases as the wave packet propagates downwards, $A_{N_t^2}$ was measured just below the region of intense isopycnal distortion where the amplitudes were close to their largest values.

Once a characteristic value for $A_{N_t^2}$ is determined, we estimate the vertical displacement amplitude, A_ξ, by assuming small-amplitude Boussinesq plane waves

https://doi.org/10.1017/S0022112004000400 Published online by Cambridge University Press

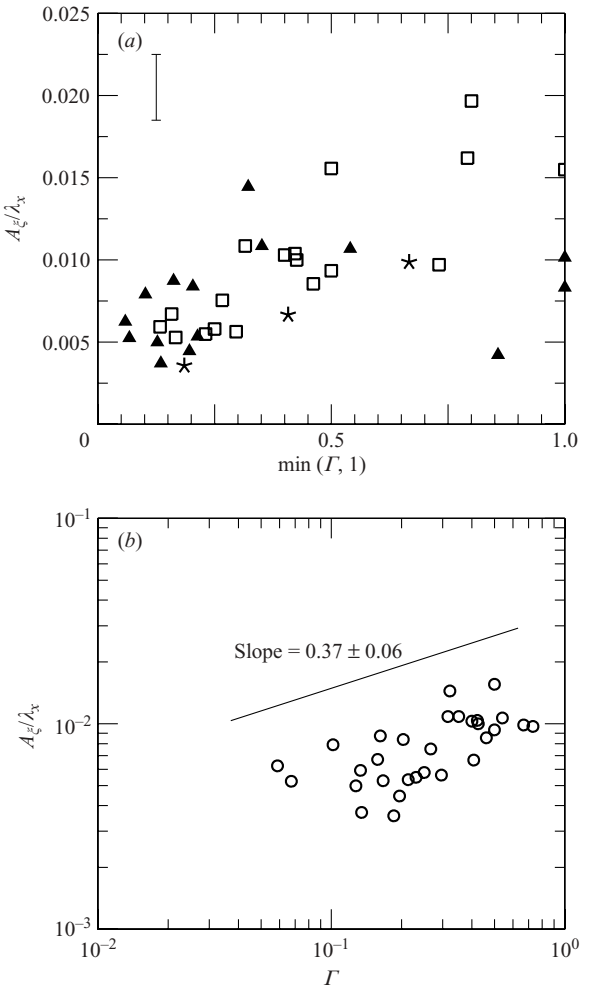


FIGURE 13. (*a*) Normalized amplitude of the vertical displacement field as a function of Γ. Data point types are □, $N^2 \simeq 0.67\,\mathrm{s}^{-2}$; *, $N^2 = 0.92\,\mathrm{s}^{-2}$; ▲, $N^2 \simeq 1.17\,\mathrm{s}^{-2}$. The error bar denotes the typical uncertainty in the measurement of A_ξ/λ_x. (*b*) Log–log plot of the same data but plotted only for those experiments with $\Gamma \leqslant 0.75$. The slope of the (vertically offset) best-fit line is indicated.

in a uniformly stratified (Sutherland *et al.* 1999):

$$A_\xi = \frac{A_{N_i^2}}{k_z \omega N^2}. \tag{5.1}$$

5.3. *Wave excitation*

The generation of internal gravity waves is due primarily to two factors: the initial collapse of the lock fluid and the forcing imparted by the head of the fluid intrusion as it propagates along the interface. Here, focus is directed only to the latter, which represents the dominant mechanism of wave generation beyond $x \simeq L_l$.

Figure 13(*a*) shows the variation of A_ξ/λ_x with Γ. There exists a relatively large degree of error associated with the measurement of A_ξ, due primarily to the high degree of background noise in the wave field (see e.g. figure 10). Consistent with the

https://doi.org/10.1017/S0022112004000400 Published online by Cambridge University Press

results of figure 8(*b*), however, a positive correlation between A_ξ/λ_x and Γ is noted for $\Gamma \lesssim 0.75$: heavier intrusions penetrate more deeply into the stratified layer and result in larger deflections to the isopycnal surfaces. This in turn yields larger-amplitude internal gravity waves. Although the large degree of scatter makes it difficult to determine the precise relation between A_ξ/λ_x and Γ, figure 9(*b*) suggests that

$$\frac{A_\xi}{\lambda_x} \propto \Gamma^{0.37\pm0.06}, \qquad \Gamma \leqslant 0.75. \tag{5.2}$$

When $\Gamma \gtrsim 0.75$, A_ξ/λ_x also depends on N^2 as a result of non-negligible interactions between the intrusion, which penetrates well below the interface, and columnar mode disturbances in the stratified lower layer.

The variation of observed wavenumber, k_x, with forcing wavenumber, $2\pi/l_i$, is shown in figure 14(*a*). Consistent with the interpretation of figure 10 as a snapshot image, the collapse of the experimental data suggests that there is a direct correlation between the scale of the intrusion head and that of the internal gravity waves it generates. Explicitly,

$$k_x = C\frac{2\pi}{l_i}, \tag{5.3}$$

where $C = 1.32 \pm 0.07$.

It is less clear that the internal gravity wave frequency is set by the frequency at which the fluid intrusion forces the stratified layer. Figure 14(*b*) plots the relative wave frequency, ω/N, against the relative forcing frequency, ω_i/N. One of the dashed lines superimposed on this plot indicates where $\omega = \omega_i$. Obviously, waves are not directly excited by the intrusion because, despite the fact that the forcing frequency lies below the buoyancy frequency, in no experiments do the wave frequencies match the intrusion frequency. We might suppose that superharmonic waves are instead excited, hence we also plot the dashed line $\omega = 2\omega_i$. Though this line passes through the data, there is considerable scatter about it in excess of the typical measurement variability.

As an alternative explanation, consider figure 15 which shows A_ξ/λ_x as a function of Θ and indicates that the most pronounced internal gravity waves propagate within a relatively narrow band of angles to the vertical, Θ, ranging between 41° and 64°. Taken together, figures 14(*a*) and 15 imply that for internal gravity waves generated by the head of an intrusion, the horizontal wavelength is determined by the size of the intrusion head whereas the frequency of propagation is established relative to the buoyancy frequency such that $\Theta \simeq 53° \pm 11°$.

This narrow frequency range has been observed in a variety of other experimental studies. In his study of wave excitation by the gravitational collapse of a mixed region in uniformly stratified surroundings, Wu (1969) found that the wave energy spectrum was sharply peaked about $\Theta \simeq 37°$. Our results are in better agreement with the studies of Linden (1975) and Dohan & Sutherland (2003), who examined waves generated beneath a turbulent mixed layer in mixing-box experiments. By observing perturbations to suspended aluminium particles, Linden estimated the dominant waves propagated at an angle of 55°. Using Fourier transform analyses of digitized time series images, Dohan & Sutherland found that waves propagated in a range of angles: $42° \leqslant \Theta \leqslant 55°$. Wave propagation in this range was also noted by Sutherland & Linden (1998) in their study of stratified flow over a thin barrier. A summary of the above results is presented in table 1.

https://doi.org/10.1017/S0022112004000400 Published online by Cambridge University Press

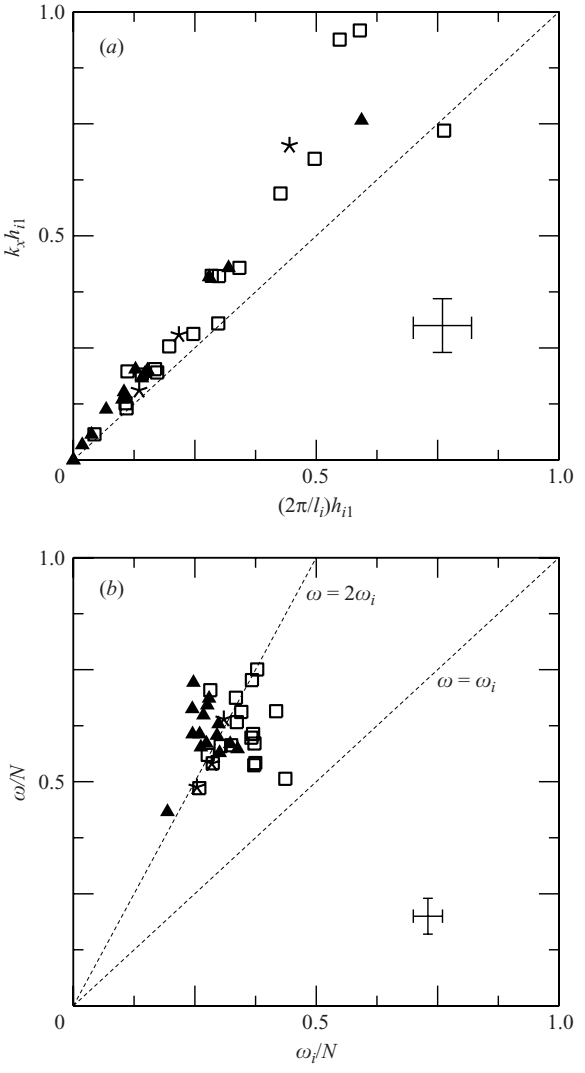


FIGURE 14. (*a*) Normalized horizontal wavenumber of the internal gravity waves versus the normalized inverse horizontal extent of the intrusion head. The dashed line indicates where $k_x = 2\pi/l_i$. (*b*) Internal gravity wave frequency as a function of the frequency of the forcing imparted by the head of the intrusion. The dashed lines indicate the lines $\omega = \omega_i$ and $\omega = 2\omega_i$, as indicated. In both cases, data point types are as indicated in figure 13; the error bars denote the typical measurement uncertainty.

Possible reasons for this frequency selection were discussed by Dohan & Sutherland (2003). They noted that waves with fixed amplitude and horizontal wavenumber have the greatest vertical flux of horizontal momentum if their frequency $\omega = N/\sqrt{2}$, that is, if $\Theta = 45°$. Thus, waves of this frequency extract momentum most efficiently from the source and so have the most significant feedback on the generation region.

5.4. *Influence of lower undulations*

Figure 16 shows ω/N as a function of the normalized frequency, ω_u/N, associated with undulations on the bottom flank of the intrusion head. The plot indicates that

https://doi.org/10.1017/S0022112004000400 Published online by Cambridge University Press

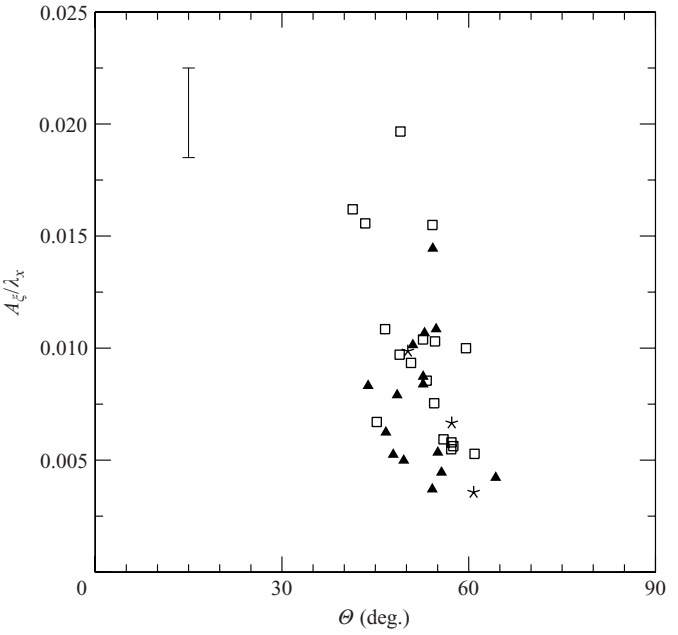


FIGURE 15. A_ξ/λ_x versus Θ. Data point types are as indicated in figure 13. The error bar denotes the typical uncertainty in the measurement of A_ξ/λ_x.

Study	Mechanism of internal gravity wave excitation	Θ
Wu (1969)	Intrusive gravity current	$\simeq 37°$
Linden (1975)	Turbulence (no mean flow)	$\simeq 55°$
Sutherland & Linden (1998)	Turbulent shear flow	45.9° to 59.9°
Dohan & Sutherland (2003)	Turbulence (no mean flow)	42° to 55°
Present study	Intrusive gravity current	41° to 64°

TABLE 1. Characteristic angle of wave propagation in five studies involving the dynamic generation of internal gravity waves.

in the vast majority of cases the undulations forced the stratified fluid at frequencies in excess of N. Furthermore, figure 16 demonstrates that ω is not a multiple of ω_u. These observations suggest that although the forcing imparted by the intrusion onto the interfacial layer results in periodic Kelvin–Helmholtz disturbances, these features are not primarily responsible for propagating internal wave excitation.

6. Discussion and conclusions

Experiments have been performed in which a fluid intrusion is released along the interface between a uniform fluid (above) and a uniformly stratified fluid (below) using a simple lock-release apparatus. Because no return flow of stratified fluid is established by releasing the lock, the generation of internal gravity waves in the stratified fluid is due solely to deflections caused by the fluid intrusion. Unlike the observations made in the related studies of Amen & Maxworthy (1980) and Maxworthy *et al.* (2002),

https://doi.org/10.1017/S0022112004000400 Published online by Cambridge University Press

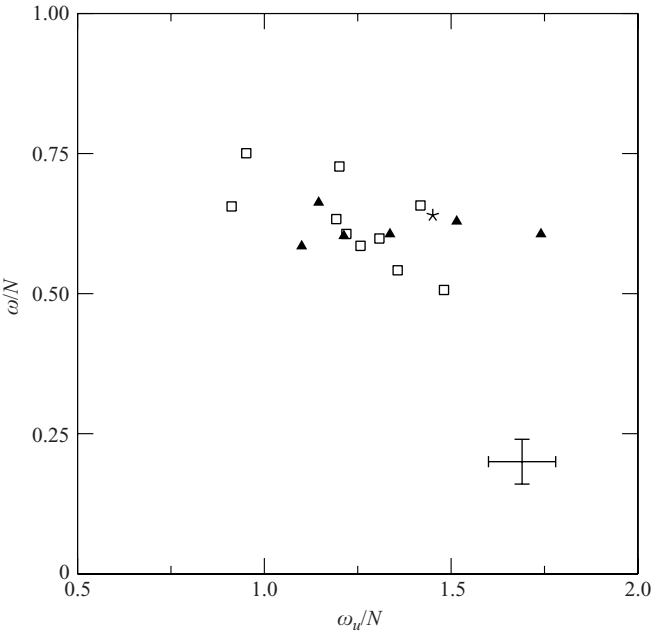


FIGURE 16. Normalized frequency of the internal gravity waves, ω, as a function of the normalized undulation frequency, ω_u. Data point types are as indicated in figure 13. The error bars denote the typical measurement uncertainty.

the intrusion's speed of propagation is essentially constant; no rhythmic interaction is established between the intrusion and the internal gravity waves.

As well as providing insight into the exact solutions of HH80, we have presented perturbation theory results in part to demonstrate the departure of the behaviour of an intrusion from that of a bottom-propagating current as the intrusion's density increases. We find that leading-order terms give estimates accurate to within 50% or better for h_{i0}, h_{i1} and v_i even when Γ is as large as 3/4. For larger Γ, the intrusion's behaviour is characterized by a dependence on N^2 and interactions with columnar modes. Such dynamics are more complex than those considered in HH80's two-layer model.

This study is motivated by a desire to assess the ability of thunderstorm outflows that propagate along the tropopause (hereinafter referred to as interfacial outflows) to excite internal gravity waves in the stratosphere. In the present set of experiments, the intrusion's plane of propagation lies above the stratified layer. The Boussinesq approximation suggests, however, that dynamically equivalent results would be obtained if, as in the atmosphere, the stratified layer were forced from below. The Boussinesq approximation is applicable because the dynamics we are interested in occur on scales well below the scale-height of the atmosphere near the tropopause (Spiegel & Veronis 1960).

As well as having non-zero mean horizontal flows, the effective density profile of the real atmosphere is far more complicated than that considered in the present set of experiments. In particular, although a density 'step' of magnitude $\sigma\rho_{00}$ was introduced between the upper and lower layers so as to minimize columnar mode excitation, the definition of σ is ambiguous in an atmospheric context (see e.g. figure 1(*b*) of Birner, Dörnbrack & Schumann 2002). Furthermore, because of the complexity of

https://doi.org/10.1017/S0022112004000400 Published online by Cambridge University Press

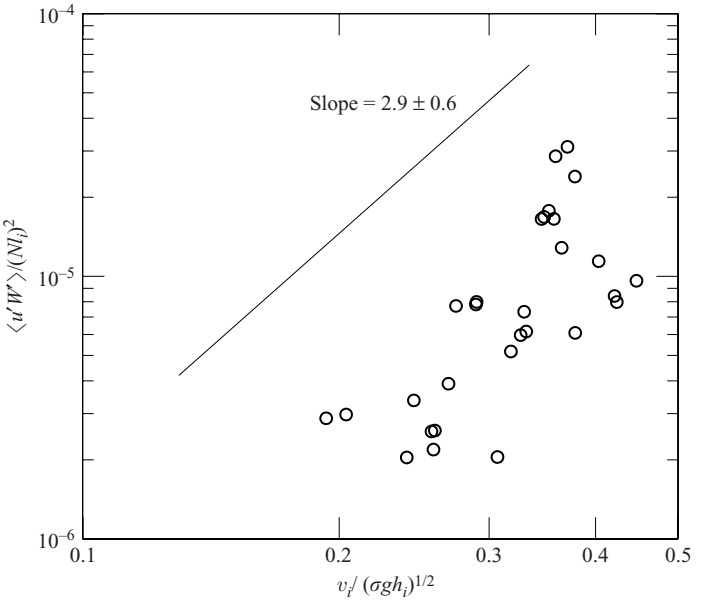


FIGURE 17. Log–log plot of the normalized momentum flux as a function of the normalized intrusion velocity for $\Gamma \leqslant 0.75$. The slope of the (vertically offset) best-fit line is indicated.

convective storm systems, interfacial outflows rarely have the appearance of a simple fluid intrusion. The precise definitions of l_i and h_i are therefore also ambiguous in many circumstances. Consequently, the results described below are intended only to provide crude estimates of the wave momentum flux associated with interfacial outflows. Further study is required to confirm the applicability of the present study to real atmospheric flows.

The characteristic period, T, of waves generated by interfacial outflows can be estimated by combining the results of table 1 with the dispersion relation for internal gravity waves (see e.g. Lighthill 1978). Taking $N \simeq 0.02\,\mathrm{s}^{-1}$ for the stratosphere (Birner *et al.* 2002), the wave period is $T \simeq 9\,\mathrm{min}$. Such high-frequency waves are known to carry a disproportionate share of the internal gravity wave momentum flux (Alexander & Pfister 1995; Dewan *et al.* 1998).

To estimate the momentum flux associated with wave generation by interfacial outflows, we seek an equation that relates $\rho_{00}\langle u'w'\rangle$ to those properties of the intrusion that are directly measurable: v_i, h_i and l_i. Explicitly, for $\Gamma \leqslant 0.75$, the collapse of the data shown in figure 17 suggests that:

$$\frac{\langle u'w'\rangle}{(Nl_i)^2} = 10^{-3.7\pm0.3}\left(\frac{v_i}{\sqrt{\sigma g h_i}}\right)^{2.9\pm0.6}. \tag{6.1}$$

We assume that $l_i = 500\,\mathrm{m}$, a representative scale for the head of an interfacial outflow (e.g. as visualized by a high-level rope cloud). For the range of normalized velocities corresponding to $\Gamma \leqslant 0.75$ (see figure 9), (6.1) predicts average values for $\rho_{00}\langle u'w'\rangle$ of between $0.2\,\mathrm{N\,m^{-2}}$ and $3\,\mathrm{N\,m^{-2}}$ depending on the values chosen for the empirical constants. By contrast, for topographically generated waves, average values for $\rho_{00}\langle u'w'\rangle$ typically range between $0.1\,\mathrm{N\,m^{-2}}$ and $1.0\,\mathrm{N\,m^{-2}}$ (e.g. see table 1 of Palmer, Shutts & Swinbank 1986).

https://doi.org/10.1017/S0022112004000400 Published online by Cambridge University Press

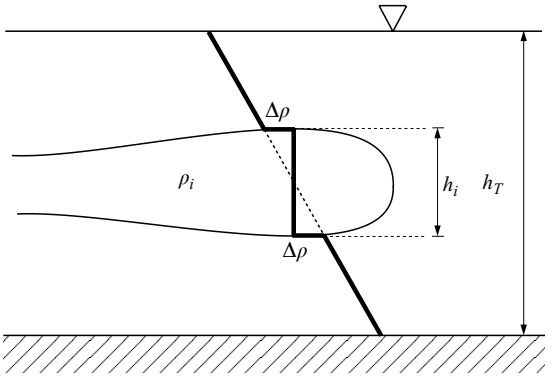


FIGURE 18. The propagation of a symmetric fluid intrusion in stratified surroundings. The density profile is indicated by the thick solid line.

The fact that the momentum flux associated with interfacial outflows is comparable to that due to topographic forcing is somewhat surprising. Whereas flow over mountains provides a spatially broad and near-continuous source of internal gravity waves, however, large-scale convective events occur sporadically, particularly in the extra-tropics. Furthermore, not all convective storms are of sufficient height to reach the tropopause. Because the stratification of the troposphere is relatively weak, outflows that travel below the tropopause are probably less effective at exciting internal gravity waves in the stratosphere. Taken together, these results suggest that in comparison with topographic forcing, wave excitation by interfacial outflows results globally in a smaller total vertical flux of horizontal momentum in the stratosphere. Locally, however, these may constitute an important source of stratospheric internal gravity waves over the tropical oceans.

We would like to thank James Rottman and reviewers of this paper for their useful comments which have helped to improve the presentation of results. Experiments reported upon here were performed in the Environmental and Industrial Fluid Dynamics Laboratory at the University of Alberta. Graduate financial support was provided by the Natural Science and Engineering Research Council (NSERC) and Alberta's iCORE program and the Canadian Foundation for Climate and Atmospheric Science. The authors would like to thank K. Yewchuck for her assistance in taking the photograph shown in figure 7.

Appendix A. Symmetric intrusion-internal wave coupling

Here, we assess theoretically under what conditions a symmetric intrusion can excite internal waves in a uniformly stratified fluid. By 'symmetric' we mean that the intrusion propagates at mid-depth with density equal to the density of the ambient at mid-depth. This circumstance has been studied experimentally by Wu (1969), Manins (1976), Amen & Maxworthy (1980).

Figure 18 shows a symmetric fluid intrusion of depth h_i and density ρ_i propagating into a uniformly stratified ambient of depth h_T. As discussed in Maxworthy *et al.* (2002), the internal gravity waves that are excited by the intrusion can propagate no faster than the linear mode-one long wave whose velocity is given by

$$v_{LW} = \frac{Nh_T}{\pi}. \tag{A 1}$$

https://doi.org/10.1017/S0022112004000400 Published online by Cambridge University Press

We compare this with the speed, v_i, of an intrusive gravity current by adapting the theory of Benjamin (1968) to a two-layer fluid. We assume the speed is controlled by the density jump, $\Delta\rho$, across the interface between the ambient and the intrusion head at its widest point, where it has depth h_i. Otherwise, we ignore the effect of the ambient stratification. Thus, in the Boussinesq approximation,

$$v_i = Fr\sqrt{\left(\frac{\Delta\rho}{\rho_{00}}\right) g h_i}, \tag{A 2}$$

where ρ_{00} is a standard reference density and the Froude number, Fr, is an order unity quantity that depends on the depth of the intrusion relative to the total depth of the domain.

Though isopycnal surfaces are compressed by the passage of the intrusion, to first order, we can approximate the density jump, $\Delta\rho$, by the change in the ambient stratification across the half-depth of the current:

$$\Delta\rho \simeq -\tfrac{1}{2}\rho'(z)h_i. \tag{A 3}$$

The intrusion speed is therefore

$$v_i \simeq \frac{Fr}{\sqrt{2}}(Nh_i) \tag{A 4}$$

Comparing this result with (A 1), we find the intrusion speed is faster than the fastest internal wave speed only if $(Fr/2^{1/2})(Nh_i) > v_{LW} = Nh_T/\pi$. That is, the system is supercritical if the Froude number exceeds $(2^{1/2}/\pi)h_T/h_i$.

In typical circumstances, $h_T \gg h_i$ and so, the Froude number being order unity, symmetric intrusions propagate as subcritical disturbances that excite internal waves.

REFERENCES

Alexander, M. J., Holton, J. R. & Durran, D. R. 1995 The gravity wave response above deep convection in a squall line simulation. *J. Atmos. Sci.* **52**, 2212–2226.

Alexander, M. J. & Pfister, L. 1995 Gravity wave momentum flux in the lower stratosphere over convection. *Geophys. Res. Lett.* **22**, 2029–2032.

Amen, R. & Maxworthy, T. 1980 The gravitational collapse of a mixed region into a linearly stratified solution. *J. Fluid Mech.* **96**, 65–80.

Baines, P. G. 1995 *Topographic Effects in Stratified Flows.* Cambridge University Press.

Becker, E. & Schmitz, G. 2002 Energy deposition and turbulent dissipation owing to gravity waves in the mesosphere. *J. Atmos. Sci.* **59**, 54–68.

Benjamin, T. B. 1968 Gravity currents and related phenomena. *J. Fluid Mech.* **31**, 209–248.

Beres, J. H., Alexander, M. J. & Holton, J. R. 2002 Effects of tropospheric wind shear on the spectrum of convectively generated gravity waves. *J. Atmos. Sci.* **59**, 1805–1824.

Birner, T., Dörnbrack, A. & Schumann, U. 2002 How sharp is the tropopause at midlatitudes? *Geophys. Res. Lett.* **29**, 10.1029/2002GL015,142.

Britter, R. E. & Simpson, J. E. 1978 Experiments on the dynamics of a gravity current head. *J. Fluid Mech.* **88**, 223–240.

Britter, R. E. & Simpson, J. E. 1981 A note on the structure of the head of an intrusive gravity current. *J. Fluid Mech.* **112**, 459–466.

Clark, T. L., Hauf, T. & Kuettner, J. P. 1986 Convectively forced internal gravity waves: results from two-dimensional numerical experiments. *Q. J. R. Met. Soc.* **112**, 899–925.

Cotton, W. R. & Anthes, R. A. 1989 *Storm and Cloud Dynamics.* Academic Press, San Diego, USA.

D'Alessio, S. J. D., Moodie, T. B., Pascal, J. P. & Swaters, G. E. 1996 Gravity currents produced by sudden release of a fixed volume of heavy fluid. *Stud. Appl. Maths* **96**, 359–385.

https://doi.org/10.1017/S0022112004000400 Published online by Cambridge University Press

D'Alessio, S. J. D., Moodie, T. B., Pascal, J. P. & Swaters, G. E. 1997 Intrusive gravity currents. *Stud. Appl. Maths* **98**, 19–46.

Dalziel, S. B. 1992 Decay of rotating turbulence: some particle tracking experiments. *Appl. Sci. Res.* **49**, 217–244.

Dewan, E. M., Picard, R. H., O'Neil, R. R., Gardiner, H. A., Gibson, J., Mill, J. D., Richards, E., Kendra, M. & Gallery, W. O. 1998 MSX satellite observations of thunderstorm-generated gravity waves in mid-wave infrared images of the upper stratosphere. *Geophys. Res. Lett*. **25**, 939–942.

Dohan, K. & Sutherland, B. R. 2003 Internal waves generated from a turbulent mixed region. *Phys. Fluids* **15**, 488–498.

Dugan, J. P., Warn-Varnas, A. C. & Piacsek, S. A. 1976 Numerical results for laminar mixed region collapse in a density stratified fluid. *Comput. Fluids* **4**, 109–121.

Faust, K. M. & Plate, E. J. 1984 Experimental investigation of intrusive gravity currents entering stably stratified fluids. *J. Hydraul. Res.* **22**, 315–325.

Fovell, R., Durran, D. & Holton, J. R. 1992 Numerical simulations of convectively generated stratospheric gravity waves. *J. Atmos. Sci.* **49**, 1427–1442.

Fritts, D. C. & Nastrom, G. D. 1992 Sources of mesoscale variability of gravity waves. Part II: Frontal, convective, and jet stream excitation. *J. Atmos. Sci.* **49**, 111–127.

Gavrilov, N. M. & Roble, R. G. 1994 The effect of gravity-waves on the global mean temperature and composition structure of the upper-atmosphere. *J. Geophys. Res.* **99**(D12), 25 773–25 780.

Hallworth, M. A., Huppert, H. E., Phillips, J. C. & Sparks, R. S. J. 1996 Entrainment into two-dimensional and axisymmetric turbulent gravity currents. *J. Fluid Mech.* **308**, 289–311.

Härtel, C., Kleiser, L., Michaud, M. & Stein, C. F. 1997 A direct numerical simulation approach to the study of intrusion fronts. *J. Engng Maths* **32**, 103–120.

Holyer, J. Y. & Huppert, H. E. 1980 Gravity currents entering a two-layer fluid. *J. Fluid. Mech.* **100**, 739–767.

Huppert, H. E. & Simpson, J. E. 1980 The slumping of gravity currents. *J. Fluid Mech.* **99**, 785–799.

Keulegan, G. H. 1957 An experimental study of the motion of saline water from locks into fresh water channels. Tech. Rep. 5168, Natl Bur. Stand.

Kida, H. A. 1984 A numerical experiment on the general circulation of the middle atmosphere with a three-dimensional model explicitly representing internal gravity waves and their breaking. *Pure Appl. Geophys.* **122**, 731–746.

Klemp, J. B., Rotunno, R. & Skamarock, W. C. 1994 On the dynamics of gravity currents in a channel. *J. Fluid Mech.* **269**, 169–198.

Lighthill, M. J. 1978 *Waves in Fluids.* Cambridge University Press. 504 pp.

Linden, P. F. 1975 The deepening of a mixed layer in a stratified fluid. *J. Fluid Mech.* **71**, 385–405.

Lindzen, R. S. 1974 Stability of a Helmholtz velocity profile in a continuously stratified infinite Boussinesq fluid – applications to clear air turbulence. *J. Atmos. Sci.* **31**, 1507–1514.

Lindzen, R. S. 1981 Turbulence and stress owing to gravity wave and tidal breakdown. *J. Geophys. Res.* **86**, 9707–9714.

Long, R. R. 1955 Some aspects of the flow of stratified fluids. III Continuous density gradients. *Tellus* **7**, 341–357.

Manins, P.C. 1976 Intrusion into a stratified media. *J. Fluid Mech.* **74**, 547–560.

Mason, P. J. & Sykes, R. I. 1982 A two-dimensional numerical study of horizontal role vortices in an inversion capped boundary layer. *Q. J. R. Met. Soc.* **108**, 801–823.

Maxworthy, T., Leilich, J., Simpson, J. & Meiburg, E. H. 2002 The propagation of a gravity current in a linearly stratified fluid. *J. Fluid Mech.* **453**, 371–394.

Mehta, A., Sutherland, B. R. & Kyba, P. J. 2002 Interfacial gravity currents: Part II – wave excitation. *Phys. Fluids* **14**, 3558–3569.

Moodie, T. B. 2002 Gravity currents. *J. Comput. Appl. Maths* **144**, 49–83.

Oster, G. 1965 Density gradients. *Sci. Am.* **213**, 70.

Palmer, T. N., Shutts, G. J. & Swinbank, R. 1986 Alleviation of a systematic westerly bias in general circulation and numerical weather prediction models through an orographic gravity drag parametrization. *Q. J. R. Met. Soc.* **112**, 1001–1039.

Plumb, R. A. & McEwan, A. D. 1978 The instability of a forced standing wave in a viscous, stratified fluid: a laboratory analogue of the quasi-biennial oscillation. *J. Atmos. Sci.* **35**, 1827–1839.

https://doi.org/10.1017/S0022112004000400 Published online by Cambridge University Press

DE ROOIJ, F. 1999 Sedimenting particle-laden flows in confined geometries. PhD thesis, University of Cambridge.

DE ROOIJ, F., LINDEN, P. F. & DALZIEL, S. B. 1999 Saline and particle-driven interfacial intrusions. *J. Fluid Mech.* **389**, 303–334.

ROSE, W. I., BLUTH, G. J. S., SCHNEIDER, D. J., ERNST, G. G. J., RILEY, C. M., HENDERSON, L. J. & MCGIMSEY, R. G. 2001 Observations of volcanic clouds in their first few days of atmospheric residence: The 1992 eruptions of Crater Peak, Mount Spurr Volcano, Alaska. *J. Geol.* **109**, 677–694.

ROTTMAN, J. W. & SIMPSON, J. E. 1983 Gravity currents produced by instantaneous releases of a heavy fluid in a rectangular channel. *J. Fluid Mech.* **135**, 95–110.

SALBY, M. L. & GARCIA, R. R. 1987 Transient response to localized episodic heating in the tropics. Part I: Excitation and short-time near-field behavior. *J. Atmos. Sci.* **44**, 458–498.

SCHOOLEY, A. H. 1967 Wake collapse in a stratified fluid. *Science* **157**, 421–423.

SCHOOLEY, A. H. & HUGHES, B. A. 1972 An experimental and theoretical study of internal waves generated by the collapse of a two-dimensional mixed region in a density gradient. *J. Fluid Mech.* **51**, 159–175.

SHIN, J. O., DALZIEL, S. B. & LINDEN, P. F. 2004 Gravity currents produced by lock exchange. *J. Fluid Mech.* (in press).

SIMPSON, J. E. 1972 Effects of lower boundary on the head of a gravity current. *J. Fluid Mech.* **53**, 759–768.

SIMPSON, J. E. 1982 Gravity currents in the laboratory, atmosphere, and ocean. *Annu. Rev. Fluid Mech.* **14**, 213–234.

SIMPSON, J. E. 1997 *Gravity Currents*, 2nd edn. Cambridge University Press.

SIMPSON, J. E. & BRITTER, R. E. 1979 The dynamics of the head of a gravity current advancing over a horizontal surface. *J. Fluid Mech.* **94**, 477–495.

SPIEGEL, E. A. & VERONIS, G. 1960 On the Boussinesq approximation for a compressible fluid. *Astrophys. J.* **131**, 442–447.

SUTHERLAND, B. R. 1996 The dynamic excitation of internal gravity waves in the equatorial oceans. *J. Phys. Oceanogr.* **26**, 3214–3235.

SUTHERLAND, B. R., CAULFIELD, C. P. & PELTIER, W. R. 1994 Internal wave generation and hydrodynamic instability. *J. Atmos. Sci.* **51**, 3261–3280.

SUTHERLAND, B. R., DALZIEL, S. B., HUGHES, G. O. & LINDEN, P. F. 1999 Visualization and measurement of internal waves by 'synthetic schlieren'. Part 1. Vertically oscillating cylinder. *J. Fluid Mech.* **390**, 93–126.

SUTHERLAND, B. R., KYBA, P. J. & FLYNN, M. R. 2004 Interfacial gravity currents in two-layer fluids. *J. Fluid Mech.* **514**, 327–353.

SUTHERLAND, B. R. & LINDEN, P. F. 1998 Internal wave generation by flow over a thin barrier. *J. Fluid Mech.* **377**, 223–252.

UNGARISH, M. & HUPPERT, H. E. 2002 On gravity currents propagating at the base of a stratified fluid. *J. Fluid Mech.* **458**, 283–301.

WU, J. 1969 Mixed region collapse with internal wave generation in a density stratified medium. *J. Fluid Mech.* **35**, 531–544.

https://doi.org/10.1017/S0022112004000400 Published online by Cambridge University Press